Multimode characterization of an optical-beam-deflection setup

Alex Fontana and Ludovic Bellon*

Laboratoire de Physique, Université de Lyon, ENS de Lyon, CNRS, 69342 Lyon, France

(Received 8 January 2024; revised 7 May 2024; accepted 17 June 2024; published 18 July 2024)

Optical beam deflection is a popular method to measure the deformation of micromechanical devices. As it measures mostly a local slope, its sensitivity depends on the location and size of the optical spot. We present a method to evaluate precisely these parameters, using the relative amplitude of the thermal noise–induced vibrations. With a case study of a microcantilever, we demonstrate the accuracy of the approach, as well as its ability to fully characterize the sensitivity of the detector and the parameters (mass and stiffness) of the resonator.

DOI: 10.1103/PhysRevApplied.22.014044

I. INTRODUCTION

To measure the minute deformations of micrometer-sized mechanical systems, such as cantilevers or membranes, optical beam deflection (OBD) [1,2] is a first-choice method: it combines ease of implementation and high sensitivity. It is used, for example, in mass sensing [3], acoustic sensing [4], chemical sensing [5], and biosensing [6], and is the ubiquitous method to measure deflection of the cantilever probe in atomic force microscopy [7,8]. Therefore, many articles are dedicated to describing its sensitivity, calibration, and limitations [9–17].

Some of the key points in assessing the sensitivity of the OBD are the laser-spot location and size on the micromechanical device. Those two parameters play an important role, especially if high-order oscillation modes are targeted. Indeed, the method is sensitive to the local slope of the reflective surface; thus, it will fail if the deformation implies a flat slope at the measurement point, or it will lose precision if the slope varies significantly under the spread of the spot [13]. Although these quantities can sometimes be precisely adjusted in the experiment, mostly they are not controlled and are hidden parameters of a global calibration procedure.

We devise in this work a precise way to estimate the spot location and size in a case study of a cantilever. We use for this purpose a single thermal-noise measurement (TNM) [18] of several resonance modes, including deformations in flexion and torsion. Since the equipartition relation prescribes the amplitude of the thermal fluctuations of these modes [19], their relative magnitude is linked to the sensitivity of the OBD for each mode, from which we derive the location and size of the spot. As an extra feature, for a well-characterized optical system or using an independent measurement, one can also deduce the cantilever mass and stiffness and the OBD sensitivity from the same single TNM.

We first present the principle of TNM for the flexural and torsional resonances of a cantilever, introducing the sensitivities that allow us to calibrate the displacements. Next, we compute an experimentally accessible quantity to deduce the position and size of the optical probe beam. We then use this method in an experiment and demonstrate how to fully characterize the OBD method (sensitivity) and the cantilever (mass and stiffness).

II. CALIBRATION-METHOD OVERVIEW

A. OBD measurement

The principle of measuring the deflection of a micro-cantilever with the OBD technique is depicted in Fig. 1. A laser beam is focused on the surface of the cantilever at a position x_0 along its longitudinal axis, and is reflected towards a four-quadrant photodiode. In a first approximation (small spot size), when the cantilever undergoes a deformation, the reflection occurs with an angle that is twice the local slope of the cantilever at x_0. We divide this angle into two components: one due to the flexion of the cantilever $\vartheta(x_0)$ (which is proportional to the vertical deflection δ) and one due to its torsion $\theta(x_0)$. After passing back through the focusing lens, the reflected beam is shifted in the x-y plane of the four-quadrant photodiode:

$$X = 2\mu F \vartheta(x_0), \quad Y = 2\mu F \theta(x_0), \qquad (1)$$

with F the focal length of the lens, X, Y the distance from the center of the sensor (with proper initial centering of the laser beam), and μ a magnification factor depending on the details of the optical system. For example, $\mu = 1$ for the optical scheme in Fig. 1 when the cantilever is

*Contact author: ludovic.bellon@ens-lyon.fr

at the focal point of the lens, but μF should be replaced by the distance from the tip to the sensor if the latter collects directly the reflected beam. Each quadrant records an incoming power—namely, A, B, C, and D—from which we evaluate two contrasts:

$$C_x \equiv \frac{(B+D)-(A+C)}{A+B+C+D}, \tag{2a}$$

$$C_y \equiv \frac{(A+B)-(C+D)}{A+B+C+D}. \tag{2b}$$

These dimensionless quantities are the raw signal available to detect the flexion and torsion of the cantilever with an OBD. In many commercial AFMs, these signals are available as voltages (typically $C_x \times 10\,\mathrm{V}$ for deflection). For small displacements, they are proportional to the spot position (X, Y) on the photodiode. Indeed, let us consider a Gaussian laser beam with the following irradiance profile at the photodetector surface:

$$I(x,y) = I_0 e^{-2\frac{(x-X)^2+(y-Y)^2}{w^2}}, \tag{3}$$

with w the $1/e^2$ radius of the beam. If the sensor size is much larger than the beam size, we directly get

$$\begin{aligned} C_x &= \mathrm{erf}\left(\frac{\sqrt{2}X}{w}\right) \approx \frac{2}{\sqrt{\pi}}\frac{\sqrt{2}X}{w} = 4\mu\sqrt{\frac{2}{\pi}}\frac{F}{w}\vartheta(x_0), \\ C_y &= \mathrm{erf}\left(\frac{\sqrt{2}Y}{w}\right) \approx \frac{2}{\sqrt{\pi}}\frac{\sqrt{2}Y}{w} = 4\mu\sqrt{\frac{2}{\pi}}\frac{F}{w}\theta(x_0). \end{aligned} \tag{4}$$

The approximation is valid for small displacements around the center of the photodiode $X_0, Y_0 = 0$, i.e., $X, Y \ll w$. Using diffraction laws for the Gaussian laser beam, we find that the ratio F/w is directly given by the beam waist w_0 at the focal point: $F/w = \pi w_0/\lambda$, where λ is the light wavelength. Eventually, the local angles are recovered at $x = x_0$ from the measured contrasts C_x and C_y.

B. Sensitivity

The next step is to infer the actual deflection δ or torsion θ at the end of the cantilever $x = L$, where the tip is located. We therefore need a model for the deformation profile along the cantilever. In Fig. 2, we plot an example of the power spectral density (PSD) of C_x and C_y acquired during a TNM on an Arrow TL8 cantilever [20] in vacuum. These PSDs can be seen as a sum of resonances with no overlap: the deformation is the superposition of the eigenmodes of the mechanical beam for the motion considered. The deflection $\delta(x,t)$ (torsion θ) can be decomposed into the solutions $\phi_n(x)$ of the Euler-Bernoulli equation [$\phi_m(x)$ of the Barr equation] (see Appendixes A and B for more details):

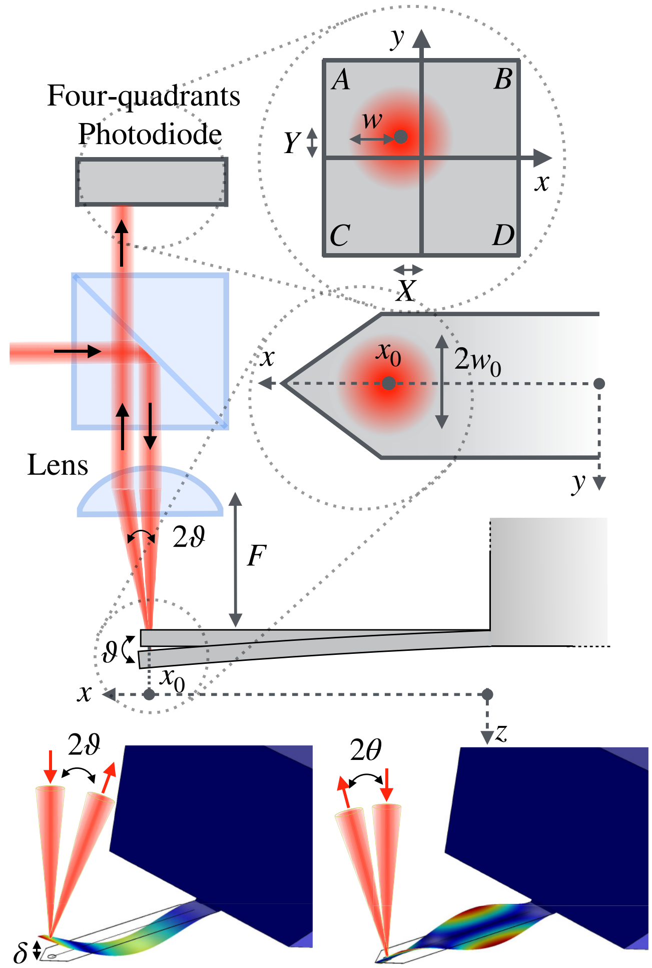

FIG. 1. Deformation of a microcantilever measured by the optical beam deflection technique: A laser beam is reflected close to the tip of the cantilever at x_0 with waist size w_0. The beam is then redirected towards a four-quadrant photodiode at the position X, Y with radius w. In the case of no displacement, the beam is centered at the sensor. If the cantilever bends, the beam is reflected with an angle. This angle corresponds to a shift in the X direction in the photodiode in the case of deflection δ and in the Y direction in the case of torsion θ.

$$\delta(x,t) = \sum_n \delta_n \phi_n(x) e^{i\omega_n t}, \tag{5}$$

$$\theta(x,t) = \sum_m \theta_m \phi_m(x) e^{i\omega_m t}, \tag{6}$$

where from now on n (m) stands for the mode number for deflection (torsion), and ω_n (ω_m) is the resonance angular frequency. For each mode, we can thus link the slopes $\vartheta(x_0,t) = \partial_x \delta(x_0,t)$ and $\theta(x_0,t)$ at position x_0 to the deformation amplitude δ_n, θ_m. Therefore, we can define the sensitivities $\sigma_n(x_0, w_0)$ and $\sigma_m(x_0, w_0)$ linking δ_n and θ_m to

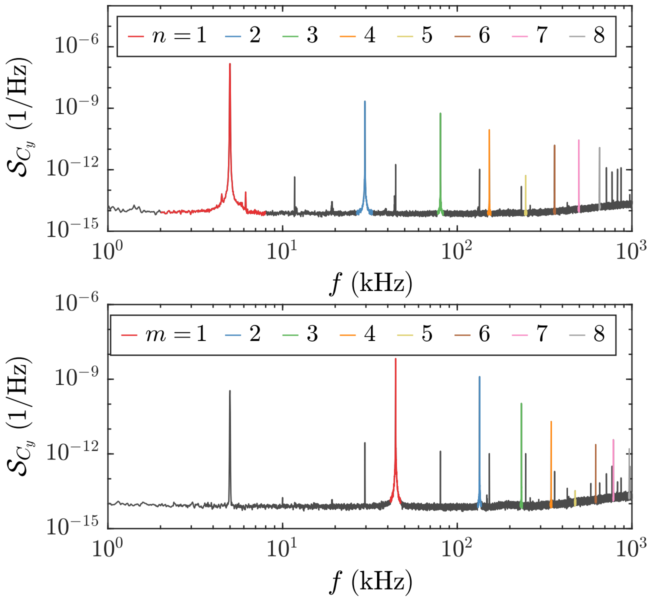

FIG. 2. (a) PSD of C_x on an Arrow TL8 cantilever [20] in vacuum. The thermal noise appears as resonance peaks at flexural frequencies f_n with no overlap. The amplitude of each one is evaluated through an integral of the PSD in a small frequency range around each resonance. (b) PSD of C_y, with the torsional resonances at f_m highlighted.

the contrast amplitudes C_n and C_m:

$$C_n = \sigma_n \delta_n, \tag{7a}$$

$$C_m = \sigma_m \theta_m, \tag{7b}$$

with

$$\sigma_n(x_0, w_0) = \frac{4\mu\sqrt{2\pi}\, w_0}{\lambda} \frac{\mathrm{d}\phi_n}{\mathrm{d}x}(x_0), \tag{8a}$$

$$\sigma_m(x_0, w_0) = \frac{4\mu\sqrt{2\pi}\, w_0}{\lambda} \phi_m(x_0). \tag{8b}$$

As shown by Eqs. (8a) and (8b), to maximize σ_n and σ_m one should maximize the laser spot radius w_0 on the cantilever [10]. Nevertheless, the approximation of a Gaussian reflected beam with an angle equal to twice the local slope at x_0 ceases to hold in this case, especially at large mode number, where the radius w_0 is comparable to the wavelength of the mode shape: the beam probes a nonuniform slope on the cantilever. To compute the flexural sensitivity σ_n in the general case, we need to compute the diffraction of the light field $E(x - x_0, y, w_0) = E_0 e^{-[(x-x_0)^2+y^2]/w_0^2}$ reflected by the cantilever. To include the effect of the triangular tip of our sample (see Fig. 1), we describe the geometry of the cantilever by its length L, uniform thickness H, and position-dependent width $W(x)$. We then follow Refs. [11,13], and show that

$$\sigma_n = \frac{4\mu}{\lambda S} \int_0^L \mathrm{d}x \int_0^L \mathrm{d}x' \int_{-\frac{\min(W(x),W(x'))}{2}}^{\frac{\min(W(x),W(x'))}{2}} \mathrm{d}y \times E(x - x_0, y, w_0) E(x' - x_0, y, w_0) \frac{\phi_n(x) - \phi_n(x')}{x - x'}, \tag{9}$$

with

$$S = \int_0^L \mathrm{d}x \int_{-\frac{W(x)}{2}}^{\frac{W(x)}{2}} \mathrm{d}y\, E(x - x_0, y, w_0)^2 \tag{10}$$

the total light power collected by the photodiode. The torsion sensitivity σ_m is similarly expressed as

$$\sigma_m = \frac{4\mu}{\lambda S} \int_0^L \mathrm{d}x\, \phi_m(x) \times \left| \int_{-\frac{W(x)}{2}}^{\frac{W(x)}{2}} \mathrm{d}y\, E(x - x_0, y, w_0) \right|^2. \tag{11}$$

The calculations are shown in Appendix E.

In the limit of small spot size w_0, the electric field contribution is equivalent to Dirac's distribution centered at x_0, so Eqs. (9) and (11) simplify to Eqs. (8a) and (8b). These formulas have a direct analogue when one is considering static deformation instead of resonant modes: we need only to replace the mode shape $\phi_n(x)$, $\phi_m(x)$ by the static deformation profile $\phi_s(x)$. The static sensitivity $\sigma_s(x_0, w_0)$ is then the one commonly calibrated in an AFM with a force curve on a hard surface (leading to the inverse optical lever sensitivity – invOLS, usually in volts per nanometer), allowing one to convert the photodetector output to a static deflection value. Once the deformation profile is set, only two parameters are needed for the calibration of the sensitivity: the laser-spot position x_0 and size w_0. Although these quantities can sometimes be measured in the experiment, we now discuss a method to retrieve them from the thermal-noise measurement itself.

C. TNM calibration

When the cantilever is in thermal equilibrium at temperature T, the equipartition principle gives

$$M\omega_n^2 \langle \delta_n^2 \rangle = k_n \langle \delta_n^2 \rangle = k_B T, \tag{12a}$$

$$J\omega_m^2 \langle \theta_m^2 \rangle = c_m \langle \theta_m^2 \rangle = k_B T, \tag{12b}$$

with M the mass and J the moment of inertia of the cantilever, k_n the stiffness of mode n, c_m the torsional stiffness of mode m, and k_B the Boltzmann constant (see

Appendix D for the derivation). The stiffness k_n can be expressed with the spatial eigenvalue α_n of mode n:

$$M\omega_n^2 \equiv k_n = \gamma K \alpha_n^4, \tag{13}$$

with K the static stiffness of the cantilever, k_n the mode stiffness, and $\gamma \sim 1/3$ a geometrical constant (see Appendix A). A similar equation can be derived for the torsional stiffness c_m. The quantities $\langle\delta_n^2\rangle$ and $\langle\theta_m^2\rangle$ represent the amplitude of fluctuations for the two deformations, i.e., the thermal content of each mode. From Eqs. (7a) and (7b), we can then write the amplitude of the measured contrasts as

$$\begin{aligned}\langle C_n^2\rangle &= \frac{\sigma_n^2(x_0,w_0)}{M\omega_n^2}k_\mathrm{B}T = \frac{\sigma_n^2(x_0,w_0)}{k_n}k_\mathrm{B}T,\\ \langle C_m^2\rangle &= \frac{\sigma_m^2(x_0,w_0)}{J\omega_m^2}k_\mathrm{B}T = \frac{\sigma_m^2(x_0,w_0)}{c_m}k_\mathrm{B}T.\end{aligned} \tag{14}$$

Experimentally, the angular frequencies $\omega_n = 2\pi f_n$ and $\omega_m = 2\pi f_m$ are easily extracted from a Lorentzian fit of the resonance in the thermal-noise spectrum (see Fig. 2). $\langle C_n^2\rangle$ ($\langle C_m^2\rangle$) is measured by integration of the PSD $\mathcal{S}_{C_x}$ ($\mathcal{S}_{C_y}$) over an adequate frequency range $2\Delta f$ around f_n (f_m):

$$\langle C_n^2\rangle = \int_{f_n-\Delta f}^{f_n+\Delta f} \mathrm{d}f\ \mathcal{S}_{C_x}(f), \tag{15a}$$

$$\langle C_m^2\rangle = \int_{f_m-\Delta f}^{f_m+\Delta f} \mathrm{d}f\ \mathcal{S}_{C_y}(f). \tag{15b}$$

During the choice of Δf and the integration one should take care to remove the contribution of the flat background noise, which is, however, negligible in most cases. From repeated measurements of the thermal-noise spectra, one can also extract the statistical uncertainty $\Delta\langle C_n^2\rangle$, $\Delta\langle C_m^2\rangle$ of the amplitude of each mode. In our experiment, $\Delta\langle C_n^2\rangle/\langle C_n^2\rangle$ decreases from 23% for mode $n=2$ to roughly 5% for higher modes for 100 spectra evaluated from 2-s-long datasets (see Appendix C).

We next define the quantities V_n^2, X_n^2, and Ω_m^2 by

$$V_n^2(\tilde{x}_0,\tilde{w}_0) \equiv \frac{\omega_n^2\langle C_n^2\rangle}{\sigma_n^2(\tilde{x}_0,\tilde{w}_0)} = \frac{k_\mathrm{B}T}{M}, \tag{16a}$$

$$X_n^2(\tilde{x}_0,\tilde{w}_0) \equiv \gamma\frac{\alpha_n^4\langle C_n^2\rangle}{\sigma_n^2(\tilde{x}_0,\tilde{w}_0)} = \frac{k_\mathrm{B}T}{K}, \tag{16b}$$

$$\Omega_m^2(\tilde{x}_0,\tilde{w}_0) \equiv \frac{\omega_m^2\langle C_m^2\rangle}{\sigma_m^2(\tilde{x}_0,\tilde{w}_0)} = \frac{k_\mathrm{B}T}{J}, \tag{16c}$$

where the second equality in each line holds when the guesses $\tilde{x}_0$ and $\tilde{w}_0$ of the position and beam radius match the experimental values x_0 and w_0. For those values then, $V_n^2(x_0,w_0)$ (X_n^2, Ω_m^2) is independent of the mode number n or m and is a velocity (deflection, angular velocity) variance common to all modes. If the calibration is performed in a fluid, the cantilever drags some material while vibrating [21]; thus, a mode-dependent mass should be considered. In this case, it is recommended to work with Eq. (16b) as the static stiffness K is mode independent. In our experiment, performed in vacuum, the mass of the cantilever M is mode independent, and the use of Eq. (16a) is equally suitable. In the following, we consider only V_n^2 and Ω_m^2.

Using the TNM, we measure the numerator of Eqs. (16a) and (16c), and using Eqs. (9) and (11), we compute the denominator as a function of $\tilde{x}_0$ and $\tilde{w}_0$. When we plot V_n^2 and Ω_m^2, all modes cross at x_0, w_0, as illustrated in Fig. 3.

To estimate the values of x_0, w_0, and M from a fitting procedure, we can minimize the following χ_M^2 function:

$$\chi_M^2(\tilde{x}_0,\tilde{w}_0,M) \equiv \sum_n\left(\frac{V_n^2(\tilde{x}_0,\tilde{w}_0)-k_\mathrm{B}T/M}{\Delta V_n^2(\tilde{x}_0,\tilde{w}_0)}\right)^2, \tag{17}$$

where ΔV_n^2 is the uncertainty on V_n^2, which is mainly due to the propagation of the statistical uncertainty of $\langle C_n^2\rangle$ through Eq. (16a) (the uncertainty on the frequency is very small). An equivalent χ_J^2 function can obviously be defined for torsion, with n and M replaced by m and J. Since Eq. (17) is quadratic in $1/M$, minimization in M can be done analytically, leading to

$$M = k_\mathrm{B}T\frac{\sum_n(\Delta V_n^2(\tilde{x}_0,\tilde{w}_0))^{-2}}{\sum_n V_n^2(\tilde{x}_0,\tilde{w}_0)(\Delta V_n^2(\tilde{x}_0,\tilde{w}_0))^{-2}}, \tag{18}$$

which can be recast in Eq. (17) to remove the dependency of χ_M^2 in M. The minimization of χ_M^2 then leads to the most probable value of $\tilde{x}_0 = x_0$ and $\tilde{w}_0 = w_0$. Since $k_\mathrm{B}T/M$ is calculated as a weighted average of V_n^2, with weights $(\Delta V_n^2)^{-2}$, the statistical uncertainty of the mass can be easily computed from

$$\mathrm{var}\left(\frac{k_\mathrm{B}T}{M}\right) = \frac{1}{\sum_n(\Delta V_n^2(\tilde{x}_0,\tilde{w}_0))^{-2}}. \tag{19}$$

In our experiment, we get a relative uncertainty of 2.7%.

Once the laser-spot position and size are known thanks to this contactless TNM, we can, in principle, easily compute all parameters of the cantilever: the mass M with Eq. (18) and the stiffness k_n of each mode with Eq. (13), from which we deduce the static stiffness K. We can also estimate the photodetector sensitivity for one vibrational mode or for a static deformation with Eq. (9). These last steps require knowledge of the optical magnification μ of the setup, which can be difficult to assess due to imprecise tuning or nonidealities (cantilever not at the focal point of the laser beam, and aberrations or aperture diffraction in the optical system). In contrast, if one of these parameters (M, K) is known from another method, it can be used to

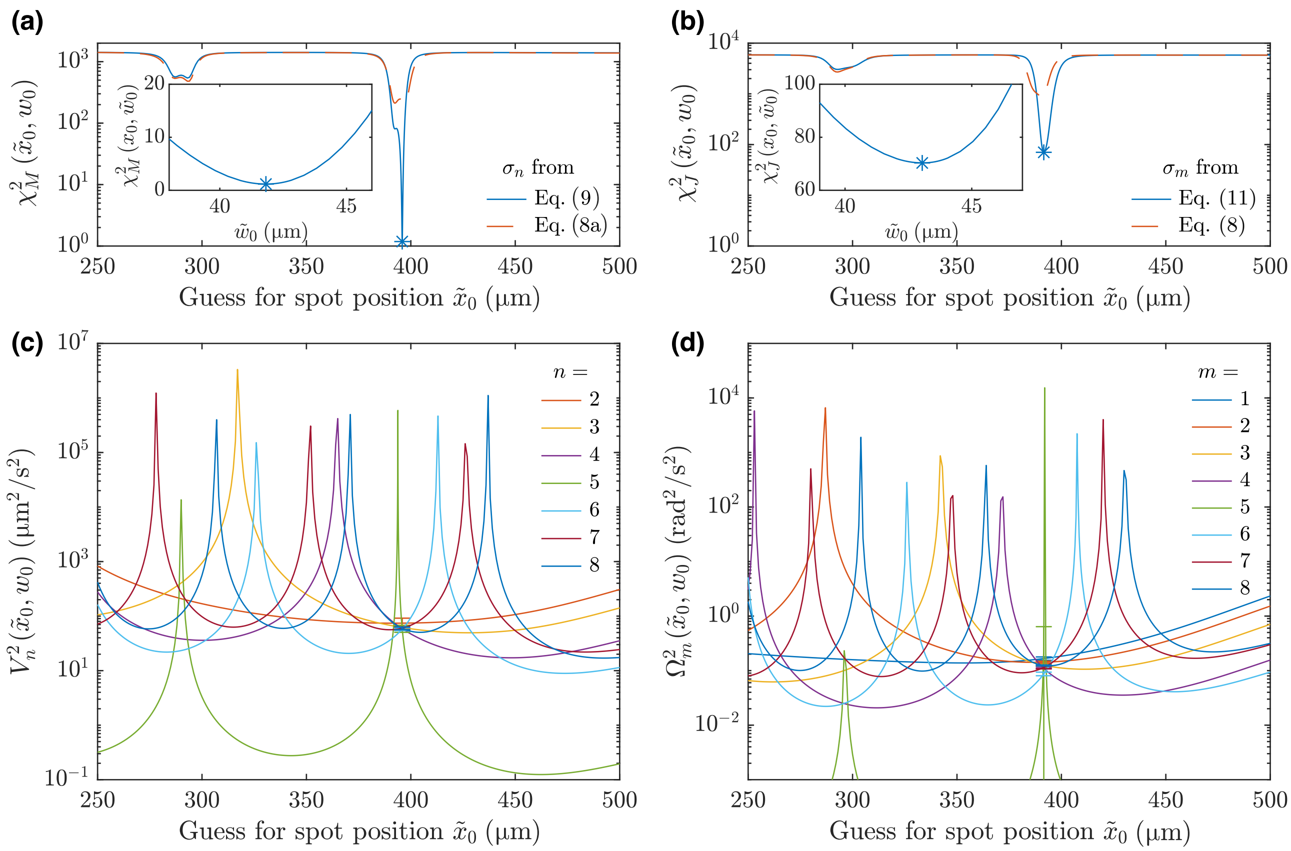

FIG. 3. Estimation of x_0 and w_0. (a) For the flexion modes, χ^2_M presents a global minimum at $x_0 = (395.9 \pm 0.2)$ µm (main figure) and $w_0 = (41.8 \pm 1.4)$ µm (inset). If the sensitivity σ_n is evaluated with the local slope model (Eq. (8b)), dashed line] instead of the diffraction integral [Eq. (9), solid line], the minimum of χ^2_M is approximately at the same position, but is far less sharp: (393 ± 5) µm. (b) The velocity variances $V^2_n(\tilde{x}_0, w_0)$, plotted here as a function of $\tilde{x}_0$ for w_0 fixed, intersect within uncertainties only at the location of the laser spot. (c) For torsion modes, χ^2_J presents a global minimum at $x_0 = (392.0 \pm 0.3)$ µm (main figure) and $w_0 = (43.0 \pm 0.9)$ µm (inset). The sharp minimum is blurred with the local slope model [Eq. (8b), dashed line] with respect to the full diffraction model for σ_m [Eq. (11), solid line]. (d) The angular velocity variances $\Omega^2_m(\tilde{x}_0, w_0)$, plotted here as a function of $\tilde{x}_0$ for w_0 fixed, intersect within uncertainties only at the location of the laser spot.

infer μ and the sensitivities of the OBD. This includes, for example, the use of the Sader model [21] in atomic force microscopy to evaluate the stiffness of the first oscillation mode k_1. Another example is given in the following section for our specific sample in vacuum (and is thus not compatible with the Sader method), with use of the resonance frequencies to determine the mass M [22].

III. EXPERIMENT

This calibration procedure was commonly used in previous work by our group to extract a calibrated measurement of the thermal noise of the cantilever [23]. We illustrate it here with an Arrow TL8 silicon cantilever [20], of length $L = 500$ µm, width $W = 95$ µm, and thickness $H \sim 1$ µm, with a triangular free end. In the experiment, we focus the probe near the tip of the cantilever with a diameter close to W, as suggested in Fig. 1.

We report in Fig. 3 the measurement of x_0 and w_0 through the minimization of χ^2, deduced from a single TNM. As we can see, χ^2 has a well-defined minimum at a certain position x_0 and radius w_0 where the velocity variance V_n or Ω_m converges for all the measured modes. For the fitted laser position x_0, we note that there is only a 1% difference between torsion and flexion. The estimated beam sizes w_0 are also very similar for the two mode families (3% difference, within uncertainties).

We exclude from the procedure the first mode in flexion ($n = 1$), whose thermal-noise amplitude is corrupted by spurious phenomena (mainly self-oscillations of the cantilever due to an optomechanical coupling [23,24]). Although it is the most prominent, mode $n = 1$ is the least sensitive to small changes in the probing position or waist, and thus its exclusion in our experiment is not problematic. Conversely, at high pressure, or with different probes, self-oscillations should not occur, and thus the first flexural resonance will most likely be available. We report the

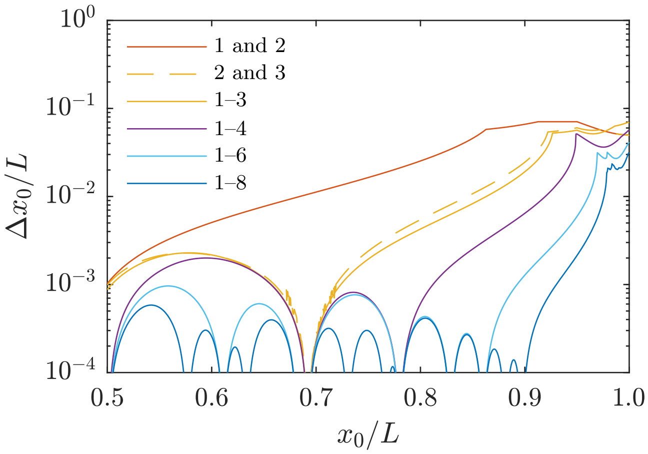

FIG. 4. Uncertainty on the estimated position Δx_0 as a function of the measurement position x_0. The curves demonstrate the effect of the number N of modes available (from 2 to 8 from top to bottom): the larger is N, the better is the precision. It can be seen that higher-order modes are the most useful, and that mode 1 has little influence on the result: use of modes 2 and 3 only (dashed yellow line) leads to a result very similar to that obtained with use of modes 1–3 (solid yellow line). The proximity of a sensitivity node is highly beneficial and lowers significantly the uncertainty. In this figure, Δx_0 is computed through error propagation of a 5% uncertainty on all $\langle C_n^2 \rangle$ using a model case corresponding to a rectangular cantilever in the limit of small detection spot size.

effect of limiting the number of resonances considered in Fig. 4.

To compute the sensitivity of our OBD, we need the value of μ, which is not well controlled in our setup, as the cantilever is not exactly in the focal plane of the lens. From the geometry of our setup and Gaussian-beam optics using the value of w_0 measured as reported above, we estimate $\mu \sim 0.5$. Instead, we use an independent measurement of the cantilever mass M to assess μ. This estimation of M is inspired by Ref. [22]: the angular resonance frequencies ω_n are linked to the spatial eigenvalues α_n of the Euler-Bernoulli equations by the dispersion relation

$$\omega_n = \sqrt{\frac{Y}{12\rho}\frac{H}{L^2}}\alpha_n^2, \tag{20}$$

where $Y = 169\,\mathrm{GPa}$ and $\rho = 2330\,\mathrm{kg/m^3}$ are the Young's modulus and the density of silicon (the material of the cantilever), respectively. Since the eigenvalues α_n are known from our computing the resonant mode ϕ_n, L is measured with an optical microscope, and the ω_n are measured in the TNM, H can be evaluated independently for all modes, yielding $H = (0.707 \pm 0.004)\,\mu\mathrm{m}$. Interestingly, the dispersion relation for the torsion modes [25] can also be used to estimate $H = (0.687 \pm 0.007)\,\mu\mathrm{m}$, in very good agreement with flexion. Our knowing the thickness, the density, and the plane geometry (L, W, triangular tip) leads to the mass $M = 6.9 \times 10^{-11}$ kg with good precision. Finally, we can adjust the magnification μ to 0.6 for Eq. (16a) to match this value.

Now that the geometry of the cantilever is known, other quantities, such as the static stiffness $K = 0.011\,\mathrm{N/m}$, or the dynamic stiffnesses k_n can be computed. The moment of inertia of the cantilever can also be evaluated as $J = 4.6 \times 10^{-20}\,\mathrm{m^2\,kg}$. It falls reasonably close to the value extracted from Eq. (16c), $J = 3.4 \times 10^{-20}\,\mathrm{m^2\,kg}$. This slight underestimation of J by the torsion modes is attributed to the difficulty in accurately describing the shape of the torsion mode ϕ_m close to the triangular tip.

IV. CONCLUSIONS

In our experiment, we take advantage of the many resonant modes that are available to achieve this calibration. To show the feasibility of such a procedure in other experimental setups, we discuss briefly two less-ideal cases. First, if the beam size is small compared with the wavelength of the highest normal mode N considered, i.e., $2w_0 < L/N$ (see Fig. 5), its estimation becomes difficult. However, in such a case w_0 has little influence on the sensitivity dependence of the modes, and can be fixed to an approximate value without it influencing the accuracy of the measurement of x_0. Use of an independent measurement of the mass then yields the sensitivity and thus the optical beam size. Second, if fewer resonances are available, the estimation of the probe's position becomes less precise (see Fig. 4). This is the case for experiments performed in fluids (decreasing the quality factor leads to lower signal-to-noise ratios) or with different kinds of cantilevers (shorter ones shift the resonances at high frequency). If N is too small, the error on the estimation of the probing point (and thus on the stiffness) will be high. It is emphasized that if the precision required on x_0 is high, then it is advisable to choose a location close to a node in sensitivity, as we did is our case study using mode 5. In general, the precision drops when x_0 is larger than the highest node available and x_0 gets close to L.

When N is sufficiently large, we end up with a full characterization of our OBD sensor. Indeed, the location and the size of the laser spot on the micromechanical resonator, the sensitivity of the measurement, and the geometry, mass, and stiffness of the cantilever are all assessed. Let us now recapitulate the calibration steps:

(1) Measure the thermal-noise amplitude of all available, say, flexural, resonances $\langle C_n^2 \rangle$ and the associated resonance frequencies ω_n.

(2) Compute the sensitivity σ_n assuming magnification $\mu = 1$.

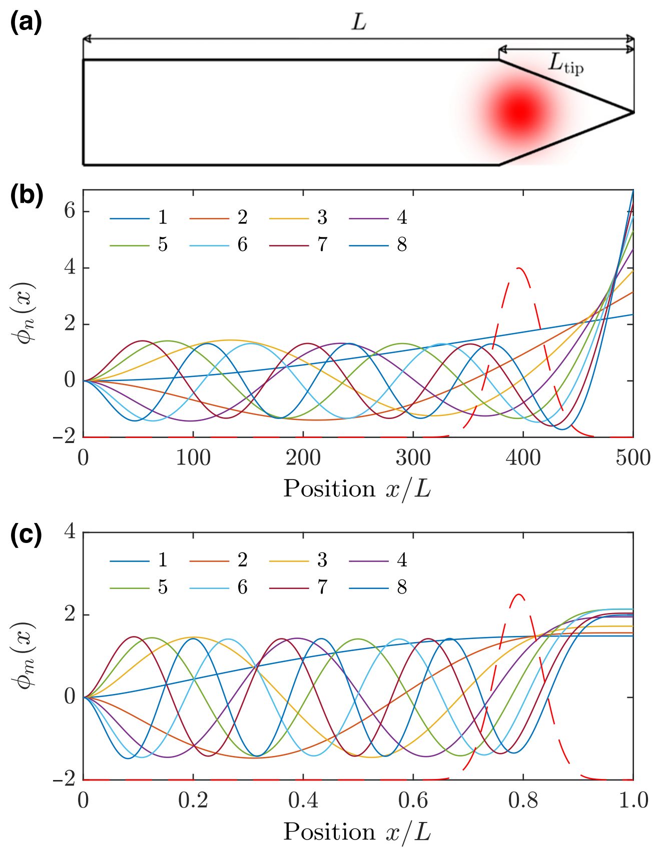

FIG. 5. Eigenmodes computed for the triangular-tipped cantilever. (a) Sketch of the cantilever (top view), with a Gaussian beam at $x_0 = 396\,\mu$m of $1/e^2$ radius $w_0 = 42\,\mu$m. The profile of this spot is plotted as the dashed red line in (b),(c). It illustrates the nonconstant slope of the high-order normal modes in the light beam. (b) $\phi_n(x)$ are the solutions of the Euler-Bernoulli equation (A1) for $n = 1$ to $n = 8$ with a nonuniform width characterized by $l_{tip} = L_{tip}/L = 0.245$. The boundary conditions are clamp-free, and are solved by numerical integration. With respect to a rectangular cantilever, the deflection of the free end is amplified by the weakening local rigidity when W decreases. (c) $\phi_m(x)$ are the solutions of Barr's equation (A1) for $n = 1$ to $n = 8$. Note that ϕ_m represents here directly the slope of the cantilever in the transverse direction, while in (b) ϕ_n is the vertical deflection, the slope of which is sensed by the OBD.

(3) Compute the velocity variance V_n^2 for a measurement in a vacuum, or the displacement variance X_n^2 for a measurement in a fluid.

(4) Minimize Eq. (17) to obtain the probing spot x_0 and beam size w_0.

(5) Extract the mass M (or the stiffness K) from an independent measurement.

(6) Deduce the actual magnification μ from Eq. (16a) and obtain the adjusted calibration function σ_n.

Following this procedure, the measurement device is fully calibrated.

As a final conclusion, we mention that we focused in this article on the OBD configuration, but the calibration of other optical detection schemes, such as interferometry, could also be assessed in the same way. In this case, the sensitivity nodes are the zeros of the eigenmodes and are closer to the tip, further expanding the method precision in detecting the probing point. Furthermore, the intrinsic calibration of the interferometer would remove the need for an independent measurement of one oscillator property.

The data that support the findings of this study and the scripts to compute mode shapes and perform all calibration steps are openly available in Ref. [26].

ACKNOWLEDGMENTS

This work was financially supported by the French région Auvergne-Rhône-Alpes through the project Dylofipo and the Optolyse platform (CPER 2016) and by the Agence Nationale de la Recherche through Grants No. ANR-18-CE30-0013 and No. ANR-22-CE42-0022. We thank Nicolas Barros for useful complementary data from a finite-element-method simulation to validate our analytical model.

APPENDIX A: DEFLECTION NORMAL MODES

The Euler-Bernoulli equation [27] for the normal modes of the cantilever vertical deflection δ can be written as

$$\left[\rho WH\frac{\partial^2}{\partial t^2} + \frac{\partial^2}{\partial x^2}Y\frac{WH^3}{12}\frac{\partial^2}{\partial x^2}\right]\delta(x,t) = 0, \qquad \text{(A1)}$$

with ρ the density of the material, Y the Young's modulus, and W and H the width and thickness of the cantilever. The following boundary conditions apply (clamp-free beam): $\delta(0,t) = 0$, $\partial_x\delta(0,t) = 0$, $\partial_x^2\delta(L,t) = 0$, and $\partial_x WH^3\partial_x^2\delta(L,t) = 0$. The triangular tip of the cantilever is taken into account by the x-dependent width $W(x)$:

$$W(x) = \min\left(\frac{L-x}{L_{tip}}W, W\right), \qquad \text{(A2)}$$

with $L = 500\,\mu$m and $L_{tip} = 82\,\mu$m for the sample in this case study. This boundary-value problem has no simple analytical solution but can be integrated numerically, yielding the eigenmodes $\phi_n(x)$ [Fig. 5(b)] and the associated spatial eigenvalue α_n (Table I).

In the straight part of the cantilever, we derive the dispersion relation between α_n and the angular resonance frequency ω_n:

$$\rho\omega_n^2 = \frac{YH^2}{12}\frac{\alpha_n^4}{L^4}. \qquad \text{(A3)}$$

The ratio of the resonance frequency and the square of the eigenvalue is thus mode independent, as seen in Eqs.

TABLE I. Computed eigenvalues of a triangular-tipped cantilever with $L_{\mathrm{tip}}/L = 0.245$, measured resonance frequency, and thickness H of our sample evaluated from the dispersion relation Eq. (A3), for deflexion modes $n = 1$ to 8. All modes yield the same results, within a 0.3% standard deviation.

Mode n	Eigenvalue α_n	Frequency (kHz) $\omega_n/2\pi$	Thickness (nm) $H = L^2\sqrt{12\rho/Y}\omega_n/\alpha_n^2$
1	2.118	4.992	711
2	5.192	29.59	701
3	8.529	80.09	703
4	11.74	152.6	708
5	14.89	246.2	710
6	18.03	360.5	709
7	21.18	496.4	707
8	24.33	652.6	705

(13) and (20). We check this prediction in Table I: the agreement is excellent, within 0.3%. The dispersion actually depends on the ratio $l_{\mathrm{tip}} = L_{\mathrm{tip}}/L$, which is finely tuned to minimize the standard deviation of the values of H. A rectangular cantilever model for example ($l_{\mathrm{tip}} = 0$) leads to an overestimation of H by 12% and a dispersion between modes of 7%. The value $l_{\mathrm{tip}} = 0.245$ we extract from this procedure is a bit larger than expected from geometry (0.17). We believe this small deviation is due to other nonidealities of the cantilever, such as a nonuniform thickness.

The geometrical factor γ in Eq. (13) can be computed with use of the expressions for the mass and static stiffness of the triangular tipped cantilever:

$$M = \rho WHL(1 - l_{\mathrm{tip}}/2), \tag{A4}$$

$$K = \frac{YWH^3}{4L^3}\frac{1}{1 + l_{\mathrm{tip}}^3/2}. \tag{A5}$$

Use of the dispersion relation [Eq. (A3)] and the definition of k_n [Eq. (13)] leads to

$$\gamma = \frac{M\omega_n^2}{K\alpha_n^4} = \frac{1}{3}\left(1 - \frac{1}{2}l_{\mathrm{tip}}\right)\left(1 + \frac{1}{2}l_{\mathrm{tip}}^3\right). \tag{A6}$$

APPENDIX B: TORSION NORMAL MODES

To describe torsion, we use the model from Ref. [25]. The vertical deflection of the normal modes $\delta(x, y, t) = \theta(x) y e^{i\omega t}$ is governed by the following coupled differential equations:

$$\frac{\partial^2\theta}{\partial x^2} = -\frac{\rho}{S}\omega^2\theta + \kappa(x)\frac{\partial\psi}{\partial x}, \tag{B1}$$

$$\frac{\partial^2\psi}{\partial x^2} = -\frac{\rho}{Y}\omega^2\psi + \frac{\kappa(x)}{\eta(x)}\left(\psi - \frac{\partial\theta}{\partial x}\right), \tag{B2}$$

TABLE II. Measured torsion resonance frequencies, and thickness H of our sample evaluated from the Barr model. All torsion modes $m = 1$ to 8 yield the same results, within a 1% standard deviation.

Mode m	Resonance frequency (kHz) $\omega_m/2\pi$	Thickness (nm) H
1	44.31	703
2	134.0	688
3	232.7	683
4	344.5	682
5	472.0	684
6	619.5	689
7	782.7	686
8	964.5	681

where $S = 51$ GPa is the shear modulus of silicon, and κ and η are functions of H and $s(x) = W(x)/H$,

$$\kappa = 1 - \frac{4}{1 + s^2}\left[1 - 6\sum_{j=0}^{\infty}\frac{\tanh \kappa_j s}{\kappa_j^5 s}\right], \tag{B3}$$

$$\eta = \frac{H^2}{1 + s^2}\left[\frac{s^2}{12} + \sum_{j=0}^{\infty}\frac{9}{\kappa_j^6}\left(\frac{\tanh \kappa_j s}{\kappa_j s} + \frac{\tanh^2 \kappa_j s}{3} - 1\right)\right], \tag{B4}$$

with $\kappa_j = (j + \frac{1}{2})\pi$ (and with the x dependency dropped to simplify the notation). The following boundary conditions apply (clamp-free beam): $\theta(0) = 0$, $\psi(0) = 0$, $\partial_x\psi(L) = 0$, and $\partial_x\theta(L) = \kappa(L)\psi(L)$. This boundary-value problem has no simple analytical solution but can be integrated numerically, yielding the eigenmodes $\phi_m(x)$ plotted in Fig. 5(c). As for flexion, using numerical integration and the experimental values of the resonance frequencies, we can estimate the thickness of the cantilever: the value agrees very well with the previous estimation, with a 1% standard deviation (Table II).

APPENDIX C: RELATIVE ERROR OF THE DISPLACEMENT

Our raw data consist of approximately 100 2-s time traces of the contrast signals C_x and C_y. For each time trace, we compute the power spectral density and extract the amplitudes, thus approximately 100 values of C_n and 100 values of C_m for each resonance mode. The mean quadratic values $\langle C_n^2\rangle$, $\langle C_m^2\rangle$ and their statistical uncertainties $\Delta\langle C_n^2\rangle$, $\Delta\langle C_m^2\rangle$ are evaluated from these approximately 100 independent estimations.

In each time trace, the amplitude of a single mode varies slowly in time, with typical correlation time $2Q_n/\omega_n$, $2Q_n/\omega_m$, which decreases with n and m. The low-frequency modes are thus probed at a lower frequency than their high-frequency counterparts, leading to a higher statistical uncertainty on their variance. Conversely, the amplitude of the thermal noise decreases with the mode number, while the floor noise slightly increases. The signal-to-noise ratio thus decreases with n and m (and if the probing point of the displacement is close to a node), thus increasing the statistical uncertainties. Overall, the relative uncertainty of all modes is similar, around 5%.

APPENDIX D: EQUIPARTITION

When the cantilever is in thermal equilibrium at temperature T, the equipartition principle implies that the mean kinetic energy of each mode is $\frac{1}{2}k_BT$, with k_B the Boltzmann constant. We can therefore write

$$\int_0^L \mathrm{d}x\, \frac{1}{2}\rho H W(x)\omega_n^2\langle\delta_n^2\rangle\phi_n^2(x) = \frac{1}{2}k_BT, \tag{D1}$$

$$\int_0^L \mathrm{d}x\, \frac{1}{2}\rho H \frac{W^3(x)}{12}\omega_m^2\langle\theta_m^2\rangle\phi_m^2(x) = \frac{1}{2}k_BT. \tag{D2}$$

We use a convenient normalization of the normal modes such that

$$\int_0^L \mathrm{d}x\, \rho H W(x)\phi_n^2(x) = \int_0^L \mathrm{d}x\, \rho H W(x) = M, \tag{D3}$$

$$\int_0^L \mathrm{d}x\, \rho H \frac{W^3(x)}{12}\phi_m^2(x) = \int_0^L \mathrm{d}x\, \rho H \frac{W^3(x)}{12} = J. \tag{D4}$$

Note that this is the common normalization of the normal modes for a rectangular cantilever where W is uniform. Our combining the last four equations leads to the equipartition expression of Eq. (12).

APPENDIX E: DIFFRACTION INTEGRAL

With the mode shapes ϕ_n, ϕ_m computed in the previous sections, we can proceed to calculation of the sensitivity of the measurement in the case of a large spot, expressed by Eqs. (7a) and (7b). Our working hypothesis is a Gaussian light field E of $1/e^2$ radius w_0 incident on the cantilever:

$$E(x-x_0, y, w_0) = E_0 e^{-\frac{(x-x_0)^2+y^2}{w_0^2}}. \tag{E1}$$

The beam reflected from the cantilever back to the sensor from point x, y travels an additional distance $2\delta(x,y)$, twice the vertical displacement of the cantilever. If δ is small, we can express the electric field E_{PD} on the photodiode through the diffraction integral [13]:

$$E_{PD}(X,Y,x_0,w_0) = \frac{k}{2\pi F}\int_0^L \mathrm{d}x \int_{-\frac{W(x)}{2}}^{\frac{W(x)}{2}} \mathrm{d}y \times E(x-x_0,y,w_0)e^{2ik\delta(x,y)}e^{-ikx\frac{X}{F}}e^{-iky\frac{Y}{F}}, \tag{E2}$$

with $k = 2\pi/\lambda$, X, Y the coordinates on the sensor, and F its distance to the cantilever (the lens collects only this light field and propagates it unchanged to the sensor if the cantilever is in its focal plane). Referring to Fig. 1, let us consider quadrant A as an example. The collected power is given by

$$A = \int_{-\infty}^0 \mathrm{d}X \int_0^\infty \mathrm{d}Y\, |E_{PD}(X,Y,x_0,w_0)|^2, \tag{E3}$$

where we assumed that the photodiode is much larger than the spread of the laser spot on its surface. For the deflection case, the measured contrast C_x [defined in Eq. (2a)] is calculated as the difference between the intensity collected in the left and right quadrants (henceforth referred to as D_x) normalized by the total intensity S. For the difference we can thus write

$$\begin{aligned} D_x = {} & \int_0^L \mathrm{d}x \int_0^L \mathrm{d}x' \int_{-\frac{W(x)}{2}}^{\frac{W(x)}{2}} \mathrm{d}y \int_{-\frac{W(x')}{2}}^{\frac{W(x')}{2}} \mathrm{d}y' \\ & \times E(x-x_0,y,w_0)E(x'-x_0,y',w_0) \\ & \times e^{2ik(\delta(x,y)-\delta(x',y'))}\frac{k}{2\pi F}\int_{-\infty}^{+\infty}\mathrm{d}Y\, e^{-ikY(y-y')/F} \\ & \times \frac{k}{2\pi F}\left(\int_0^{+\infty} - \int_{-\infty}^0\right)\mathrm{d}X\, e^{-ikX(x-x')/F}. \end{aligned} \tag{E4}$$

The integral over X yields a Cauchy principal part ($\mathbb{P}$) and the integral over Y yields a Dirac's δ δ^D:

$$\begin{aligned} & \frac{k}{F}\left(\int_0^{+\infty} - \int_{-\infty}^0\right)\mathrm{d}X\, e^{-ikX(x-x')/F} = \mathbb{P}\frac{2i}{x-x'}, \\ & \int_{-\infty}^{+\infty}\mathrm{d}Y\, e^{-ikY(y-y')/F} = -\delta^D(y-y'). \end{aligned} \tag{E5}$$

Furthermore, for small displacements we can write

$$e^{2ik(\delta(x,y)-\delta(x',y'))} \approx 1 + 2ik\left(\delta(x,y)-\delta(x',y')\right). \tag{E6}$$

In this case, D_x reads

$$\begin{aligned} D_x = {} & \frac{1}{i\pi}\mathbb{P}\int_0^L \mathrm{d}x \int_0^L \mathrm{d}x' \int_{-\frac{W(x)}{2}}^{\frac{W(x)}{2}} \mathrm{d}y \int_{-\frac{W(x')}{2}}^{\frac{W(x')}{2}} \mathrm{d}y' \\ & \times E_c(x-x_0,y,w_0)E_c(x'-x_0,y',w_0) \\ & \times \frac{1+2ik(\delta(x,y)-\delta(x',y'))}{x-x'}\delta^D(y-y'). \end{aligned} \tag{E7}$$

The zeroth order of the displacement contribution is zero because the integrand is antisymmetric with respect to x and x'. Furthermore, the principal part of the integral is dropped, as the integrand is not singular in $x = x'$. We consider the contribution of the flexion mode n $\delta(x,y) =$

$\delta_n\phi_n(x)$ [from Eq. (5)], which is independent of y. We then insert δ into Eq. (E7) and integrate the Dirac's δ, but now D_x is renamed D_n (specific to mode n):

$$D_n = \frac{4\delta_n}{\lambda}\int_0^L \mathrm{d}x \int_0^L \mathrm{d}x' \int_{-\frac{\min\left(W(x),W(x')\right)}{2}}^{\frac{\min\left(W(x),W(x')\right)}{2}} \mathrm{d}y \times E(x-x_0,y,w_0)E(x'-x_0,y,w_0) \times \frac{\phi_n(x)-\phi_n(x')}{x-x'}. \tag{E8}$$

Similarly, the sum of all the photodiodes S can be deduced from Eq. (E4):

$$S = \int_0^L \mathrm{d}x \int_0^L \mathrm{d}x' \int_{-\frac{W(x)}{2}}^{\frac{W(x)}{2}} \mathrm{d}y \int_{-\frac{W(x')}{2}}^{\frac{W(x')}{2}} \mathrm{d}y' \times E(x-x_0,y,w_0)E(x'-x_0,y',w_0) \times e^{2ik(\delta(x,y)-\delta(x',y'))}\frac{k}{2\pi F}\int_{-\infty}^{+\infty}\mathrm{d}X\, e^{-ikX(x-x')/F} \times \frac{k}{2\pi F}\int_{-\infty}^{+\infty}\mathrm{d}Y\, e^{-ikY(y-y')/F}. \tag{E9}$$

In this case the zeroth order of the displacement contribution is nonzero due to the integral being symmetric, and thus S is independent of the mode considered, as expected. Calculating the integrals, Eq. (E9) simplifies to

$$S = \int_0^L \mathrm{d}x \int_{-\frac{W(x)}{2}}^{\frac{W(x)}{2}} \mathrm{d}y\, E(x-x_0,y,w_0)^2. \tag{E10}$$

From Eqs. (E8) and (E10) it is then possible to express the contrast $C_n = D_n/S$:

$$C_n = \frac{4\delta_n}{\lambda S}\int_0^L \mathrm{d}x \int_0^L \mathrm{d}x' \int_{-\frac{W(x)}{2}}^{\frac{W(x)}{2}} \mathrm{d}y \times E(x-x_0,y,w_0)E(x'-x_0,y,w_0) \times \frac{\phi_n(x)-\phi_n(x')}{x-x'} = \sigma_n(x_0,w_0)\delta_n, \tag{E11}$$

which gives the sensitivity of Eq. (7a).

In the same way, we can recover the torsional sensitivity. From Eq. (2b), the contrast C_m is the difference between the upper and lower quadrants. Following the procedure used to retrieve C_n, we consider the torsion mode m in Eq. (6): $\delta(x,y) = \theta_m y\phi_m(x)$. The difference between the left and right quadrants is given by

$$D_m = \frac{4\theta_m}{\lambda}\int_0^L \mathrm{d}x\, \phi_m(x) \times \left|\int_{-\frac{W(x)}{2}}^{\frac{W(x)}{2}} \mathrm{d}y\, E(x-x_0,y,w_0)\right|^2. \tag{E12}$$

The contrast then reads

$$C_m = \frac{4\theta_m}{\lambda S}\int_0^L \mathrm{d}x\, \phi_m(x) \times \left|\int_{-\frac{W(x)}{2}}^{\frac{W(x)}{2}} \mathrm{d}y\, E(x-x_0,y,w_0)\right|^2 = \sigma_m(x_0,w_0)\theta_m, \tag{E13}$$

which gives the torsional sensitivity of Eq. (11).

[1] R. V. Jones, Some developments and applications of the optical lever, J. Sci. Instrum. **38**, 37 (1961).
[2] G. Meyer and N. M. Amer, Novel optical approach to atomic force microscopy, Appl. Phys. Lett. **53**, 1045 (1988).
[3] S. Dohn, R. Sandberg, W. Svendsen, and A. Boisen, Enhanced functionality of cantilever based mass sensors using higher modes, Appl. Phys. Lett. **86**, 233501 (2005).
[4] D. Ren and Z.-M. Qi, An optical beam deflection based MEMS biomimetic microphone for wide-range sound source localization, J. Phys. D: Appl. Phys. **54**, 505403 (2021).
[5] N. Lavrik, M. Sepaniak, and G. D. Panos, Cantilever transducers as a platform for chemical and biological sensors, Rev. Sci. Instrum. **75**, 2229 (2004).
[6] J. Tamayo, P. M. Kosaka, J. J. Ruz, A. San Paulo, and M. Calleja, Biosensors based on nanomechanical systems, Chem. Soc. Rev. **42**, 1287 (2013).
[7] F. J. Giessibl, Advances in atomic force microscopy, Rev. Mod. Phys. **75**, 949 (2003).
[8] H.-J. Butt, B. Cappella, and M. Kappl, Force measurements with the atomic force microscope: Technique, interpretation and applications, Surf. Sci. Rep. **59**, 1 (2005).
[9] C. A. J. Putman, B. G. De Grooth, N. F. Van Hulst, and J. Greve, A detailed analysis of the optical beam deflection technique for use in atomic force microscopy, J. Appl. Phys. **72**, 6 (1992).
[10] M. G. L. Gustafsson and J. Clarke, Scanning force microscope springs optimized for optical beam deflection and with tips made by controlled fracture, J. Appl. Phys. **76**, 172 (1994).
[11] T. E. Schäffer and P. K. Hansma, Characterization and optimization of the detection sensitivity of an atomic force microscope for small cantilevers, J. Appl. Phys. **84**, 4661 (1998).
[12] R. W. Stark, Optical lever detection in higher eigenmode dynamic atomic force microscopy, Rev. Sci. Instrum. **75**, 5053 (2004).

[13] T. E. Schäffer, Calculation of thermal noise in an atomic force microscope with a finite optical spot size, Nanotechnology **16**, 664 (2005).

[14] T. Fukuma, M. Kimura, K. Kobayashi, K. Matsushige, and H. Yamada, Development of low noise cantilever deflection sensor for multienvironment frequency-modulation atomic force microscopy, Rev. Sci. Instrum. **76**, 053704 (2005).

[15] L. Y. Beaulieu, M. Godin, O. Laroche, V. Tabard-Cossa, and P. Grütter, Calibrating laser beam deflection systems for use in atomic force microscopes and cantilever sensors, Appl. Phys. Lett. **88**, 083108 (2006).

[16] L. Beaulieu, M. Godin, O. Laroche, V. Tabard-Cossa, and P. Grütter, A complete analysis of the laser beam deflection systems used in cantilever-based systems, Ultramicroscopy **107**, 422 (2007).

[17] R. Herfst, W. Klop, M. Eschen, T. van den Dool, N. Koster, and H. Sadeghian, Systematic characterization of optical beam deflection measurement system for micro and nanomechanical systems, Measurement **56**, 104 (2014).

[18] H. J. Butt and M. Jaschke, Calculation of thermal noise in atomic force microscopy, Nanotechnology **6**, 1 (1995).

[19] P. Paolino, B. Tiribilli, and L. Bellon, Direct measurement of spatial modes of a microcantilever from thermal noise, J. Appl. Phys. **106**, 094313 (2009).

[20] NanoWorld, Switzerland.

[21] J. E. Sader, Frequency response of cantilever beams immersed in viscous fluids with applications to the atomic force microscope, J. Appl. Phys. **84**, 64 (1998).

[22] J. Lübbe, L. Doering, and M. Reichling, Precise determination of force microscopy cantilever stiffness from dimensions and eigenfrequencies, Meas. Sci. Technol. **23**, 045401 (2012).

[23] A. Fontana, R. Pedurand, and L. Bellon, Extended equipartition in a mechanical system subject to a heat flow: the case of localised dissipation, J. Stat. Mech. **2020**, 073206 (2020).

[24] A. Fontana, R. Pedurand, V. Dolique, G. Hansali, and L. Bellon, Thermal noise of a cryocooled silicon cantilever locally heated up to its melting point, Phys. Rev. E **103**, 062125 (2021).

[25] A. D. S. Barr, Torsional waves in uniform rods of non-circular section, J. Mech. Eng. Sci. **4**, 127 (1962).

[26] A. Fontana and L. Bellon, Dataset and scripts for "Multimode characterization of an optical beam deflection setup" [Data set]. Zenodo. https://doi.org/10.5281/zenodo.11110784 (2024).

[27] L. Landau and E. Lifshitz, *Theory of Elasticity*, Course of Theoretical Physics, Vol. 7 (Elsevier Science, 1970).